

# Measuring short-range correlations and quasi-elastic cross sections in $A(e,e')$ at $x > 1$ and modest $Q^2$

Y.P. Zhang<sup>a</sup>, Z.H. Ye<sup>a,b</sup>, D. Nguyen<sup>b</sup>, P. Aguilera<sup>c</sup>, Z. Ahmed<sup>d</sup>, H. Albataineh<sup>e</sup>, K. Allada<sup>f</sup>, B. Anderson<sup>g</sup>, D. Anez<sup>h</sup>, K. Aniol<sup>i</sup>, J. Annand<sup>j</sup>, J. Arrington<sup>k,l</sup>, T. Averett<sup>m</sup>, H. Baghdasaryan<sup>b</sup>, X. Bai<sup>n</sup>, A. Beck<sup>o</sup>, S. Beck<sup>o</sup>, V. Bellini<sup>p</sup>, F. Benmokhtar<sup>q</sup>, A. Camsonne<sup>f</sup>, C. Chen<sup>f</sup>, J.-P. Chen<sup>f</sup>, K. Chirapatpimol<sup>b</sup>, E. Cisbani<sup>s</sup>, S. Covrig Dusa<sup>f</sup>, M. M. Dalton<sup>f,t</sup>, D. Day<sup>b</sup>, W. Deconinck<sup>u</sup>, M. Defurne<sup>v</sup>, D. Flay<sup>w</sup>, N. Fomin<sup>x</sup>, M. Friend<sup>y</sup>, E. Fuchey<sup>w</sup>, F. Garibaldi<sup>s</sup>, D. Gaskell<sup>f</sup>, S. Gilad<sup>u</sup>, R. Gilman<sup>z</sup>, S. Glamazdin<sup>aa</sup>, C. Gu<sup>b</sup>, P. Guèye<sup>f</sup>, C. Hanretty<sup>b</sup>, J.-O. Hansen<sup>f</sup>, M. Hashemi Shabestari<sup>b</sup>, D. W. Higinbotham<sup>f</sup>, M. Huang<sup>ab</sup>, S. Iqbal<sup>i</sup>, G. Jin<sup>b</sup>, N. Kalantarians<sup>b</sup>, H. Kang<sup>ac</sup>, A. Kelleher<sup>u</sup>, I. Korover<sup>ad</sup>, J. LeRose<sup>f</sup>, J. Leckey<sup>ae</sup>, S. Li<sup>af</sup>, R. Lindgren<sup>b</sup>, E. Long<sup>g</sup>, J. Mammei<sup>ag</sup>, P. Markowitz<sup>ah</sup>, D. Meekins<sup>f</sup>, R. Michaels<sup>f</sup>, M. Mihovilović<sup>ai</sup>, N. Muangma<sup>u</sup>, C. Munoz Camacho<sup>aj</sup>, B. E. Norum<sup>b</sup>, Nuruzzaman<sup>ak</sup>, K. Pan<sup>u</sup>, S. Phillips<sup>af</sup>, E. Piasetzky<sup>ad</sup>, I. Pomerantz<sup>ad,al</sup>, M. Posik<sup>w</sup>, V. Punjabi<sup>am</sup>, X. Qian<sup>ab</sup>, Y. Qiang<sup>f</sup>, X. Qiu<sup>an</sup>, P. E. Reimer<sup>l</sup>, A. Rakhman<sup>d</sup>, S. Riordan<sup>b,ao</sup>, G. Ron<sup>ap</sup>, O. Rondon-Aramayo<sup>b</sup>, L. Selvy<sup>g</sup>, A. Shahinyan<sup>aq</sup>, R. Shneor<sup>ad</sup>, S. Širca<sup>ar,ai</sup>, K. Slifer<sup>af</sup>, N. Sparveris<sup>w</sup>, R. Subedi<sup>b</sup>, V. Sulkosky<sup>u</sup>, D. Wang<sup>b</sup>, J. W. Watson<sup>g</sup>, L. B. Weinstein<sup>as</sup>, B. Wojtsekhowski<sup>f</sup>, S. A. Wood<sup>f</sup>, I. Yaron<sup>ad</sup>, J. Zhang<sup>f</sup>, Y. W. Zhang<sup>g</sup>, B. Zhao<sup>m</sup>, X. Zheng<sup>b</sup>, P. Zhu<sup>at</sup>, R. Zielinski<sup>af</sup>

<sup>a</sup>Department of Physics, Tsinghua University, Beijing, China

<sup>b</sup>University of Virginia, Charlottesville, Virginia 22904

<sup>c</sup>Institut de Physique Nucleaire (UMR 8608), CNRS/IN2P3 - Université Paris-Sud, France

<sup>d</sup>Syracuse University, Syracuse, New York 13244

<sup>e</sup>Texas A&M University - Kingsville, Kingsville, Texas, 78363

<sup>f</sup>Thomas Jefferson National Accelerator Facility, Newport News, Virginia 23606

<sup>g</sup>Kent State University, Kent, Ohio 44242

<sup>h</sup>Saint Mary's University, Halifax, Nova Scotia, Canada

<sup>i</sup>California State University, Los Angeles, CA 90032

<sup>j</sup>University of Glasgow, Glasgow, Scotland, UK

<sup>k</sup>Lawrence Berkeley National Laboratory, Berkeley, California

<sup>l</sup>Physics Division, Argonne National Laboratory, Argonne, Illinois

<sup>m</sup>College of William & Mary, Williamsburg, Virginia

<sup>n</sup>China Institute of Atomic Energy, Beijing, China

<sup>o</sup>Nuclear Research Center Negev, Beer-Sheva, Israel

<sup>p</sup>Università di Catania, Italy

<sup>q</sup>Duquesne University, Pittsburgh, PA

<sup>r</sup>Hampton University, Hampton, Virginia

<sup>s</sup>INFN, Sezione Sanità and Istituto Superiore di Sanità, Rome, Italy

<sup>t</sup>Ohio University, Athens, Ohio

<sup>u</sup>Massachusetts Institute of Technology, Cambridge, MA

<sup>v</sup>CEA Saclay, Gif-sur-Yvette, France

<sup>w</sup>Temple University, Philadelphia, Pennsylvania

<sup>x</sup>University of Tennessee, Knoxville, TN

<sup>y</sup>Carnegie Mellon University, Pittsburgh, PA

<sup>z</sup>Rutgers University, Piscataway, New Jersey

<sup>aa</sup>Kharkov Institute of Physics and Technology, Ukraine

<sup>ab</sup>Duke University, Durham, North Carolina

<sup>ac</sup>Seoul National University, Korea

<sup>ad</sup>Tel Aviv University, Israel

<sup>ae</sup>Indiana University, Bloomington, Indiana

<sup>af</sup>University of New Hampshire, Durham, NH

<sup>ag</sup>Virginia Tech, Blacksburg, Virginia

<sup>ah</sup>Florida International University, Miami, Florida

<sup>ai</sup>Jozef Stefan Institute, Ljubljana, Slovenia

<sup>aj</sup>Université Blaise Pascal/IN2P3, France

<sup>ak</sup>Mississippi State University, Starkville, MS

<sup>al</sup>The University of Texas at Austin, Austin, Texas

<sup>am</sup>Norfolk State University, Norfolk, Virginia

<sup>an</sup>Lanzhou University, China

<sup>ao</sup>University of Massachusetts, Amherst, Massachusetts

<sup>ap</sup>Hebrew University of Jerusalem, Israel

<sup>aq</sup>Yerevan Physics Institute, Armenia

<sup>ar</sup>Faculty of Mathematics and Physics, University of Ljubljana, Slovenia

<sup>as</sup>Old Dominion University, Norfolk, Virginia

<sup>at</sup>University of Science and Technology, Hefei, China

arXiv:2504.17462v1 [nucl-ex] 24 Apr 2025

## Abstract

We present results from the Jefferson Lab E08-014 experiment, investigating short-range correlations (SRC) through measurements of absolute inclusive quasi-elastic cross sections and their ratios. This study utilized 3.356 GeV electrons scattered off targets including  $^2\text{H}$ ,  $^3\text{He}$ ,  $^4\text{He}$ ,  $^{12}\text{C}$ ,  $^{40}\text{Ca}$ , and  $^{48}\text{Ca}$ , at modest momentum transfers ( $1.3 < Q^2 \lesssim 2 \text{ GeV}^2$ ). Kinematics were selected to enhance the cross-section contribution from high-momentum nucleons originating from the strongly interacting, short-distance components of two-nucleon SRCs (2N-SRCs), known to exhibit a universal structure across both light and heavy nuclei. We analyzed the  $A^2/H$  ratio within the region dominated by 2N-SRCs to characterize the nuclear dependence of SRC contributions across various nuclei. Additionally, the  $A^3/\text{He}$  ratio was examined at kinematics sensitive to nucleons with even higher momentum, aiming to identify signals indicative of three-nucleon SRCs (3N-SRCs). The traditional analysis method in the expected 3N-SRC region ( $x > 2$ ) did not yield a clear plateau; instead, the data diverged from the predicted 3N-SRC behavior as momentum transfer increased. However, when analyzed in terms of the struck nucleon's light-cone momentum, the data exhibited the opposite trend, progressively approaching the predicted 3N-SRC plateau. These observations suggest that future measurements at higher energies may facilitate a definitive isolation and identification of 3N-SRCs.

## 1. Introduction

Short-range correlations (SRCs) are configurations of nucleons with large relative momenta and modest total momentum. They are dominated by two-nucleon SRCs (2N-SRC) but may have significant contributions from three-nucleon SRCs (3N-SRC) in specific kinematic regimes. These correlations arise from ephemeral fluctuations in the nuclear ground state, driven by the strong, short-range component of the nucleon-nucleon (NN) interaction, which includes both an attractive tensor force and a deep repulsive core at sub-fm distances. Unlike the mean-field potential derived from models such as the shell model, SRCs exhibit universal characteristics across all nuclei. They contribute to the high-momentum tails observed in nucleon momentum distributions and the depletion of spectral strength seen in exclusive electron scattering experiments [1, 2, 3, 4]. A comprehensive study of SRCs is essential for a deeper understanding of nuclear forces and the detailed structure of atomic nuclei. Significant progress has been made in both theoretical and experimental investigations in recent years [2, 5, 6, 7, 8, 9, 10].

SRCs have been studied extensively through quasi-elastic (QE) electron scattering, where high-energy electron beams knock high-momentum nucleons out of nuclei at large momentum transfer [2, 10]. Inclusive electron scattering experiments,  $A(e,e')$ , which measure only the scattered electrons, have been conducted at SLAC [11] and Jefferson Lab (JLab) [12, 13, 14, 15, 16, 17, 18, 19, 20], confirming the basic predictions of the SRC model [5, 11] and quantifying the relative contribution of SRCs in nuclei [9, 10]. Exclusive measurements of QE reactions, which reconstruct back-to-back high-momentum nucleons from the breakup of 2N-SRC pairs in addition to detecting the scattered electron, have demonstrated a dominance of proton-neutron (pn) pairs over proton-proton (pp) or neutron-neutron (nn) pairs [21, 22, 23, 24, 25]. This dominance is a manifestation of the strong tensor force, which preferentially binds pn pairs, making them more likely to form SRCs [26, 27, 7, 28]. The observed pn dominance was confirmed in inclusive studies of nuclei with similar mass but different neutron-to-proton ratios, such as  $^{48}\text{Ca}/^{40}\text{Ca}$  [18] and  $^3\text{He}/^3\text{H}$  [19]. While

this isospin dependence is a universal feature in heavier nuclei, recent results suggest a weaker preference for pn pairs in light nuclei [19].

The first evidence for 2N-SRCs came from inclusive QE cross section ratios of nuclei to deuterium ( $A^2/H$ ), which revealed a distinct plateau in the region  $1.4 < x < 2.0$  [11] at  $Q^2 \gtrsim 1.4 \text{ GeV}^2$ . Here,  $Q^2$  is the four-momentum transfer squared, and  $x$  is the Bjorken variable, both of which are determined from the beam energy ( $E_0$ ) and the measured scattered electron momentum ( $E'$ ) and angle ( $\theta_e$ ). In this framework,  $Q^2 = 4E_0E' \sin^2(\theta_e/2)$  and  $x = Q^2/(2m_p\nu)$ , where  $m_p$  is the proton mass and  $\nu = E_0 - E'$ . Following this pioneering study, extensive measurements at JLab [15, 17, 19, 20] revealed the predicted 2N-SRC dominance [5, 11] and verified the kinematic conditions for which 2N-SRCs dominate over mean-field contributions. The value of the  $A^2/H$  ratio in the plateau region, denoted  $a_2(A)$ , reflects the relative contribution of SRCs in heavier nuclei compared to the deuteron. However, the motion of SRCs in nuclei with  $A > 2$  enhances the cross section ratio by  $\sim 10\text{--}20\%$  above what is predicted by simply counting SRCs [15, 29]. This enhancement increases with nuclear mass ( $A$ ), indicating a greater prevalence of nucleons in SRC pairs in heavier nuclei due to increased nucleon-nucleon interactions in denser nuclear environments, with the trend saturating at  $A \geq 12$  [3].

The  $A^3/\text{He}$  cross section ratios also exhibit the predicted 2N-SRC plateau [13, 14, 15, 16], but the SRC model also predicts a second plateau corresponding to the onset of 3N-SRCs above  $x = 2$ . For 2N-SRCs, the model predicts that SRCs dominate for momenta above the typical mean-field momenta in nuclei, while for 3N-SRCs, it is less clear when 2N-SRC contributions are small enough that the 3N-SRC contributions can be isolated. The predicted 3N-SRC plateau appeared to be observed in the  $^4\text{He}/^3\text{He}$  ratio at  $x \geq 2.25$  and  $Q^2 \sim 1.6 \text{ GeV}^2$  by CLAS [14], while a Hall C experiment at  $Q^2 \sim 2.7 \text{ GeV}^2$  reported a similar trend, albeit with large statistical uncertainties [15, 30]. However, the hypothesis that 3N-SRCs dominated at  $Q^2 \approx 1.6 \text{ GeV}^2$  and large  $x$  was ruled out by the initial publication of the present results [16], with the limited momen-

tum resolution of the CLAS spectrometer being the apparent cause of the observed plateau [31]. It has been argued that further searches for the onset of 3N-SRCs should focus on high-statistics measurements at large  $Q^2$  values ( $Q^2 \gtrsim 3 \text{ GeV}^2$ ) [9, 30, 32, 33]. It has also been suggested that focusing on very light nuclei, in particular  $^3\text{H}$  and  $^3\text{He}$ , may provide easier access to information on 3N-SRCs [20]. At this time, the existence of 3N-SRCs remains an open question that warrants further investigation [34, 10, 33] and only limited information on their structure exists [35, 20].

## 2. Experimental Overview and Data Analysis

This paper reports the results from the JLab E08-014 experiment, which measured scattered electrons and extracted inclusive QE cross section distributions for  $1 \lesssim x < 3.0$  and moderate  $Q^2$  values [36]. The previously published  $^4\text{He}/^3\text{He}$  ratio revealed the absence of the predicted 3N-SRC signal [16], while the  $^{48}\text{Ca}/^{40}\text{Ca}$  ratio provided the first examination of the isospin effect in 2N-SRCs using the inclusive scattering [18]. Here, we present the absolute cross sections for all nuclei measured in this experiment, including  $^2\text{H}$  and  $^{12}\text{C}$  targets in addition to  $^4\text{He}$ ,  $^3\text{He}$ ,  $^{48}\text{Ca}$  and  $^{40}\text{Ca}$ . We also present the  $A/2\text{H}$  and  $A/3\text{He}$  ratios to explore 2N-SRCs and 3N-SRCs.

JLab experiment E08-014 [37] utilized a 3.356 GeV unpolarized electron beam with currents ranging from 40 to 120  $\mu\text{A}$ , provided by the Continuous Electron Beam Accelerator Facility (CEBAF). The beam was directed onto several cryogenic targets, including  $^2\text{H}$ ,  $^3\text{He}$ , and  $^4\text{He}$ , which were housed in 20 cm aluminum cells. These cells were mounted on a vertically adjustable ladder within a vacuum chamber. Solid foil targets, including  $^{12}\text{C}$ ,  $^{40}\text{Ca}$ , and  $^{48}\text{Ca}$ , were positioned below the cryogenic targets. The entire target ladder was cooled to 20 K using a cryotarget cooling system [38].

Two high-resolution magnetic spectrometers (HRS-L and HRS-R) [38] were used to measure the quasi-elastically scattered electrons. Each spectrometer consists of two quadrupoles (Q1 and Q2), a dipole (D), and a final quadrupole (Q3). The magnetic fields of these components were set to match the standard optics tune for the desired central momentum value [38]. However, the Q3 magnet on HRS-R encountered a power supply issue, resulting in a 15% reduction in the field. This necessitated the acquisition of new optics data and the recalibration of the optics matrices offline to accurately account for the mismatch in the Q3 field (see Chapter 4 in Ref. [36]).

The detector setup in each HRS includes two vertical drift chambers (VDCs), two scintillator hodoscope planes (S1 and S2), a gas Cherenkov counter (GC), and two layers of electromagnetic calorimeters (CAL). The VDCs track charged particles exiting from Q3, allowing the determination of their momenta and angles at the reaction points using the HRS magnet optics. The signals from S1, S2, and GC formed triggers for the events recorded by the data acquisition (DAQ) system, with scalers monitoring detection efficiencies and computer dead time. The GC and CAL also serve as particle identification (PID) detectors to differentiate between electrons and pions.

Data were taken with the spectrometers positioned at angles between  $21^\circ$  and  $28^\circ$ , with one or more momentum settings at each angle to cover a wide range of  $x$ . Detailed kinematic settings can be found in the supplemental materials [39].

### 2.1. Electron Reconstruction and Selection

The HRS spectrometers detected scattered electrons as well as other particles, primarily  $\pi^-$  mesons. The Hall A standard offline data analysis reconstructed the scattered electron momentum ( $P_e$ ), in-plane and out-of-plane angles ( $\phi_e$ ,  $\theta_e$ ), and vertex position ( $Z_e$ ) using the VDC track information and optics reconstruction matrices [38]. For the HRS-R, the reconstruction matrices from previous experiments were updated to correct for the reduced Q3 magnetic field [36].

To minimize uncertainties associated with the spectrometer acceptance, in particular for the long targets, strict acceptance cuts were applied:  $|\delta P_e| \leq 4\%$ ,  $|\delta\theta_e| \leq 30 \text{ mrad}$ , and  $|\delta\phi_e| \leq 30 \text{ mrad}$ . For gas targets, an additional cut of  $|\delta Z_e| \leq 7 \text{ cm}$  was implemented to exclude events originating from the target entrance and exit windows. Residual contamination was evaluated using data collected from measurements with two thick aluminum foils designed to replicate the target windows. These studies indicate negligible contamination mixing with genuine gas target events ( $<0.1\%$ ) from window events due to reconstruction inaccuracies. It is worth noting that in Ref. [18], only the short targets ( $^{40}\text{Ca}$  and  $^{48}\text{Ca}$ ) were included, allowing for slightly wider acceptance cuts and smaller statistical uncertainties. Calibrated gas Cherenkov and calorimeter signals were used to apply particle identification (PID) cuts, achieving over 99% efficiency for identifying electrons, with negligible pion contamination (see Sec. 5.5.3 of Ref. [36]).

### 2.2. Non-uniform Target Density Calibration

The target cooling system served to reduce density fluctuations in the cryogenic targets and protect the foil targets from beam-induced heating. However, since only one end of the 20 cm extended target cells was mounted on the cooled ladder, non-uniform density fluctuations, often referred to as boiling effects, were observed across the cryogenic targets. Fluid dynamic simulations indicated the presence of a temperature gradient along the cells, contributing to this density variability, as shown in Fig. 1. To quantify this effect, a dedicated study was conducted to determine the in-beam total target thickness for various beam currents.

First, current dependence data were obtained for all cryogenic targets under the same kinematic settings, with beam currents ranging from  $10\mu\text{A}$  up to the maximum allowed value for the target. Next, the experimental yield distributions along the  $Z_e$  axis were divided into 60 bins over the length of the target. In each bin, we extracted the normalized yield as a function of beam current,  $Y(Z_i)/Y_0 = (1 - B_i \cdot I)$ , where  $B_i$ , referred to as the boiling factor, represents the magnitude of target-density fluctuation in the  $i$ th bin when the beam is on, and  $Y_0$  is the yield in the absence of boiling effect. This  $Z_e$ - and  $I$ -dependent density reduction is applied to  $\rho_0$ , the nominal target density measured before the target was installed.

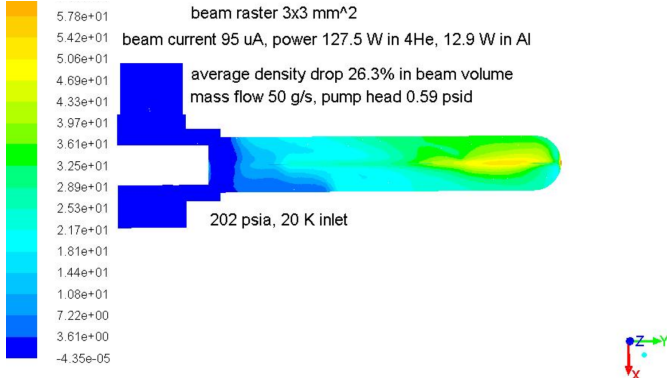


Figure 1: Fluid dynamics simulation of the  $^4\text{He}$  cryotarget cell showing density vs position. Higher densities are seen on the upstream side of the target which closer to the coolant system.

For the data analysis, we generate events in the Monte Carlo simulation using the extracted  $Z_e$ -dependent density profile for the average beam current of the setting. This allows us to simulate the impact of any  $Z_e$  dependent effects, e.g. in the spectrometer acceptance. Note that the integrated luminosity is normalized to the nominal target thickness with no beam, as a  $Z_e$ -dependent correction is applied to the data to remove the boiling effect. Figure 2 shows the simulated density distributions for  $^4\text{He}$  at  $15\mu\text{A}$  and  $95\mu\text{A}$ , compared to that extracted from the current-dependence measurements as well as the production measurement at  $95\mu\text{A}$ , showing good agreement between data and simulation. For further details, see Appendix D of Ref. [36]. A systematic uncertainty of 5% was assigned to the absolute cryotarget thicknesses to account for the final determination of the target densities. Additional uncertainties associated with imperfect modeling of the  $Z_e$  dependence are included as well, as discussed in Sec. 3.1.

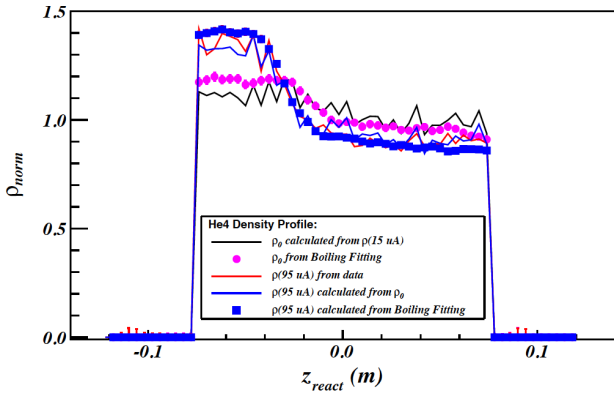


Figure 2: Comparison between real and simulated target density distributions for  $^4\text{He}$  along the reaction vertex. The black (red) line representing the real data at  $15\mu\text{A}$  ( $95\mu\text{A}$ ) and the blue line is calculated by implementing the boiling effect at  $95\mu\text{A}$  to the black line. The cyan (blue) dots are the simulated data after introducing the boiling effect at  $15\mu\text{A}$  ( $95\mu\text{A}$ ) to the original flat distributions.

### 2.3. Cross Section Extraction

For each setting, we binned the data in  $x$  bins and extracted the Born cross section by applying the ratio of the experimental

to simulated yield as a correction to the model cross section used in the simulation:

$$\sigma_{EX}(x_i, \theta_0) = Y_{EX}^i / Y_{MC}^i \cdot \sigma_{model}(x_i, \theta_0), \quad (1)$$

where the experimental (model) differential cross section in the  $i$ th bin is given as  $\sigma_{EX(model)}(x_i)$  and  $x_i$  is the central value of the bin and  $\theta_0$  is the central angle of the spectrometer.

The experimental yield,  $Y_{EX}^i$ , is defined as:

$$Y_{EX}^i = \frac{N_{EX}^i}{N_e \eta_{Ig} \epsilon_{eff}}, \quad (2)$$

where  $N_{EX}^i$  is the number of scattered electrons in the  $x$  bin after applying acceptance and particle identification (PID) cuts, and has also been corrected for computer dead-time.  $N_e = Q_e/e$  represents the total number of incoming electrons, derived from the accumulated beam charge used to acquire the data. The areal density of scattering centers is given as:  $\eta_{Ig} = \rho \cdot \Delta L_{Ig} \cdot N_a/A$ , where  $\rho$  is the target density,  $\Delta L_{Ig}$  is the target length,  $N_a$  is Avogadro's number, and  $A$  is the atomic mass number. For cryogenic targets,  $\rho \cdot \Delta L_{Ig}$  has been corrected for the non-uniform boiling effect as described in the previous section. The detection efficiency,  $\epsilon_{eff}$ , includes the efficiencies for triggering, tracking, and PID. The analysis shows that these efficiencies are consistently above 99%, allowing us to set  $\epsilon_{eff} = 1$  with a 1% systematic uncertainty.

The Monte Carlo yield,  $Y_{MC}^i$ , is defined as:

$$Y_{MC}^i = \frac{\Delta E'_{MC} \Delta \Omega_{MC}}{N_{MC}^{gen}} \cdot \sum_{j \in i} \sigma_{model}^{rad}(x_j), \quad (3)$$

where  $\Delta E'_{MC}$  and  $\Delta \Omega_{MC}$  are the ranges of scattered electron energies and solid angles defined by the same acceptance cuts applied to the real data, and  $N_{MC}^{gen}$  is the total number of generated Monte Carlo (MC) events. The differential cross section,  $\sigma_{model}^{rad}(x_j)$ , where  $j$  refers to the  $j$ th simulated event in the  $i$ th  $x$  bin, is calculated using the XEMC model (Appendix B of Ref. [36]) and includes the radiative effects [40, 41]. These effects account for random energy losses of the incoming and scattered electrons as they pass through the target and detector materials. See Ref. [41] for a comparison of these radiative correction procedures to other approaches. The summation runs over all simulated events in the  $i$ th  $x$  bin, applying the same selection criteria as in the experimental data.

The yield-ratio method uses the simulation to account for HRS and detector acceptance, bin centering, and radiative effects. This relies on having a reliable cross section model, and so after the cross section is extracted using a starting cross section model [15], the model is adjusted to match the data so that the cross section weighting used to evaluate acceptance, radiative corrections, etc. in the simulation is more realistic. This process is repeated until the simulated yield from the updated cross section model is in good agreement with the data.

## 3. Results

### 3.1. Absolute Cross Sections

Figure 3 shows the absolute differential cross section distributions as a function of  $x$  for all targets measured in this experi-

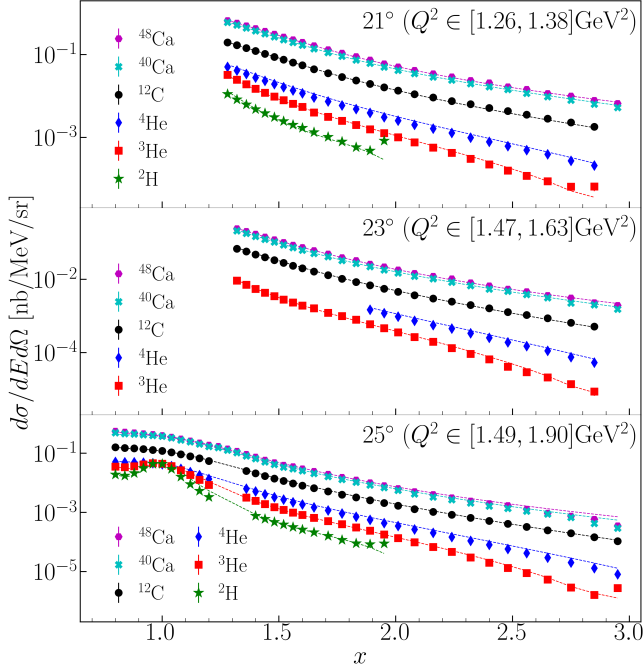


Figure 3: Differential cross sections for all nuclear targets for different scattering angles. Scale uncertainties are not shown.

ment at scattering angles of  $21^\circ$ ,  $23^\circ$ , and  $25^\circ$ . The quasi-elastic cross section for  $^2\text{H}$  should drop rapidly as  $x$  approaches the kinematic limit ( $x \approx 2$ ) but the total cross section rises due to contributions from e-d elastic scattering. Similarly,  $^3\text{He}$  shows an excess near  $x = 3$ , again indicative of nuclear elastic scattering. The lines are the XEMC cross section model [36], showing excellent agreement with the data, except for  $x \approx A$ , as the model does not include nuclear elastic scattering. Figure 4 shows the  $^3\text{He}$  and  $^{12}\text{C}$  cross sections for all angles.

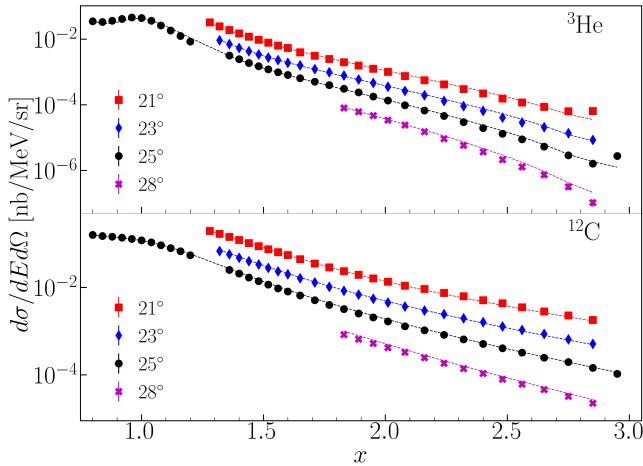


Figure 4: Differential cross sections for  $^3\text{He}$  and  $^{12}\text{C}$  targets at all angles. Scale uncertainties are not shown.

The uncertainties presented in Figures 3 and 4 include the combined statistical and uncorrelated (point-to-point, p2p) systematic uncertainties. Additionally, each data subset (angle-target combination) has an associated scale uncertainty, which allows for the rescaling of all data points. The scale and p2p uncertainties are summarized in Table 1, where the entries corre-

	$\delta\sigma/\sigma$ (scale)	$\delta\sigma/\sigma$ (p2p)
$\delta_{acc}$	2%	1.5%
$\delta_{track}$	1%	0.3%
$\delta_{PID}$	0.3%	0.1%
$\delta_{model}$	-	1.0%
$\delta_{charge}$	0.7%	-
$\delta_{dt}$	0.7%	-
$\delta_{target}$	5% (1%)	1.5-3.0% (0%)
$\delta_{rad}$	1.5% (1%)	1.0% (0.5%)
$\delta_{kin}$	1%	1.5-6% (1.5-3)%

Table 1: Systematic uncertainties for absolute cross sections. Where two values are given, the first is for the long targets ( $^2\text{H}$ ,  $^3\text{He}$ , and  $^4\text{He}$ ), and second (in parentheses) is for the short targets. See text for details of entries that quote a range of values that depend on  $x$ .

spond to the uncertainty associated with various sources: spectrometer acceptance ( $\delta_{acc}$ ), tracking efficiency ( $\delta_{track}$ ), particle identification cuts ( $\delta_{PID}$ ), model dependence of the cross section extraction ( $\delta_{model}$ ), target thickness ( $\delta_{target}$ ), beam charge measurement ( $\delta_{charge}$ ), electronic and computer dead-time ( $\delta_{dt}$ ), and radiative corrections ( $\delta_{rad}$ ). For  $\delta_{target}$ , the extended targets have larger uncertainties associated with the beam heating effects discussed in the previous section, and an additional p2p uncertainty associated with the combination of a  $Z_e$ -dependent density and uncertainty in the extended-target acceptance. The p2p uncertainty of  $\delta_{target}$  for long targets increases linearly from 1.5% to 3% as  $x$  increases from 1.4 to 2, and continues this linear increase beyond  $x = 2$ . The  $\delta_{kin}$  term accounts for the variation of cross section within the uncertainties of the beam and scattered electron energies and angles. These are similar for all targets and all  $x$  values, but increase at larger  $x$  where the cross section drops rapidly, especially for the  $^2\text{H}$  data approaching  $x = 2$ . The p2p uncertainty of  $\delta_{kin}$  for short targets has a linear increase from 1.5% to 3% as the value of  $x$  increases from 1.5 to 1.8. For long targets, the p2p uncertainty of  $\delta_{kin}$  also increases linearly, ranging from 1.5% to 6% except for  $^2\text{H}$  whose uncertainty reaches 10% when  $x = 1.8$ . In both cases, the  $\delta_{kin}$  uncertainty continues to increase linearly beyond  $x = 1.8$  at the rate described above. The extracted cross sections and fractional uncertainties are provided in the supplemental materials [39].

### 3.2. $A^2H$ Cross Section Ratios

We next form the cross section ratios of heavier nuclei to  $^2\text{H}$  to investigate the 2N-SRC plateau across different nuclei. To focus on the previously observed 2N-SRC scaling region ( $Q^2 \geq 1.4 \text{ GeV}^2$ ,  $x \geq 1.4$ ) [10, 20], we excluded the  $21^\circ$  data, as it falls within the low- $Q^2$  range. Since there was no  $23^\circ$  data for  $^2\text{H}$ , the  $A^2H$  ratios come entirely from the  $25^\circ$  data. In constructing the target ratios, several systematic uncertainties common to all targets partially or completely cancel out in the  $A^2H$  ratios. In particular, scale uncertainties associated with the experimental setup and data analysis—such as  $\delta_{acc}$ ,  $\delta_{track}$ ,  $\delta_{PID}$ , and  $\delta_{model}$ —almost entirely cancel in the ratios. A summary of the scale and point-to-point (p2p) uncertainties in the target ratios is provided in Table 2.

	$\delta R/R$ (scale)	$\delta R/R$ (p2p)
$\delta_{acc}$	2% (1s)	0.5% (1s)
$\delta_{track}$	0.2%	0.2%
$\delta_{PID}$	-	0.1%
$\delta_{model}$	-	1.0%
$\delta_{charge}$	1.0%	-
$\delta_{dt}$	0.5%	-
$\delta_{target}(s/l)$	5%	1.5-3.0%
$\delta_{target}(s/s)$	4%	1.5-3.0%
$\delta_{target}(l/l)$	1.4%	0%
$\delta_{rad}(s/l, s/s)$	1.5%	1%
$\delta_{rad}(l/l)$	0.5%	0.3%
$\delta_{kin}(A/D)$	0.6%	1.5-6.0%
$\delta_{kin}(other)$	0.6%	0.7-1.4%

Table 2: Systematic uncertainties for the cross section ratios. In some cases, the uncertainty depends on the target ratios being taken: s/s, l/l, and s/l refer to the ratio of two short targets, two long targets, or the ratio of a short to long target, respectively, while A/D refer to the ratio of any target to deuterium. The entries that quote a range of values refer to a linear increase in uncertainty with respect to  $x$ , as in Table 1.

While we have thus far used  $x$  as a surrogate for the initial struck nucleon's momentum, the light-cone momentum fraction,  $\alpha$ , provides a more accurate estimate of the initial momentum [5, 11, 10]. The light-cone momentum  $\alpha$  cannot be reconstructed from inclusive scattering without making an assumption about the unmeasured final state, but  $\alpha_{2N}$  [11] is typically used as the experimental estimate of  $\alpha$  in the mean-field and 2N-SRC regimes, based on the assumption that the momentum of the struck nucleon is balanced by one other nucleon:

$$\alpha_{2N} = 2 - \frac{q_{\min} + 2M}{2M} \left( 1 + \frac{\sqrt{W^2 - 4M^2}}{W} \right) \quad (4)$$

where  $q_{\min} = \nu - |\vec{q}|$ ,  $W^2 = \sqrt{-q^2 + 4M\nu + 4M^2}$ .

Fig. 5 shows the  $A/{}^2\text{H}$  cross section ratios as functions of  $x$  (top) and  $\alpha_{2N}$  (bottom), with a gap in coverage for  $1.2 < x < 1.4$  ( $1.12 < \alpha_{2N} < 1.18$ ). Above  $x \approx 1.7$  ( $\alpha_{2N} \approx 1.33$ ), the ratios show a slight increase, reflecting an enhanced cross section for  $A > 2$  targets due to smearing from the center-of-mass motion of the 2N-SRC pairs, as seen in previous studies [15]. As  $x$  approaches 2, the ratio begins to drop due to the contribution of the deuteron elastic peak. This effect is more pronounced than in higher- $Q^2$  data [15] due to the larger elastic contribution at these  $Q^2$  values.

For the light nuclei, a clear plateau is observed for  $\alpha_{2N} > 1.18$ , with minimal deviations until the effects discussed above begin to modify the ratio above  $\alpha_{2N} \approx 1.33$ . In contrast, for the heavier nuclei, there is an approximate plateau, but the increase at larger  $\alpha_{2N}$  values is more pronounced compared to previous measurements. We attribute this difference to variations in the acceptance between the thin ( $< 1$  cm) foil targets and the 20 cm cryotargets. Modeling the latter is more challenging in this measurement due to the large, strongly position-dependent target heating effects.

As discussed in the introduction, the  $A/{}^2\text{H}$  ratio in the plateau region, denoted as  $a_2(A)$ , represents the relative contribution of

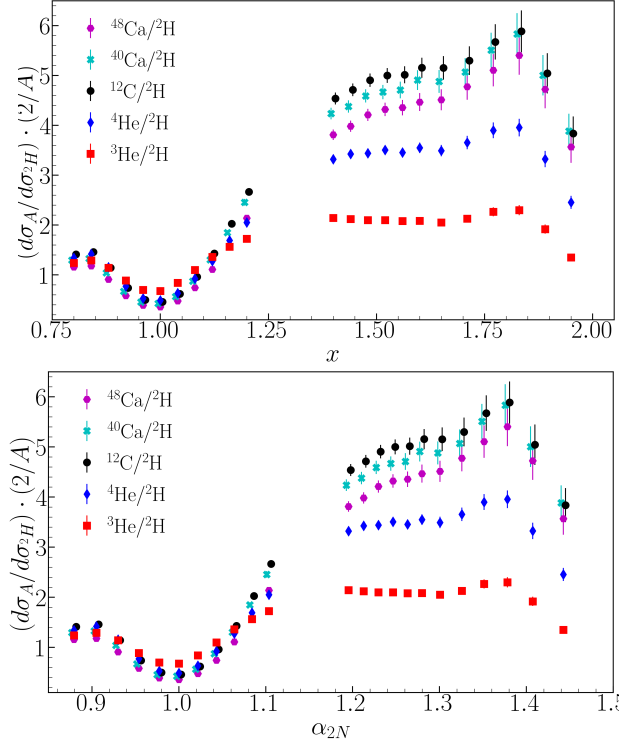


Figure 5: The  $A/{}^2\text{H}$  ratio of the cross section per nucleon as a function of  $x$  (top) and  $\alpha_{2N}$  (bottom) for the  $25^\circ$  data. Scale uncertainties are not shown. The points for  ${}^{12}\text{C}$  ( ${}^{40}\text{Ca}$ ) are shifted slightly to the right (left) so they can be more easily distinguished.

Nuclei	${}^3\text{He}$	${}^4\text{He}$	${}^{12}\text{C}$	${}^{40}\text{Ca}$	${}^{48}\text{Ca}$
$a_2$	2.103	3.455	4.859	4.554	4.163
$\delta a_2$ (fit)	0.010	0.032	0.085	0.091	0.099
$\delta a_2$ (scale)	0.041	0.068	0.279	0.261	0.239

Table 3: The extracted values of  $a_2$  and uncertainties from the present data.  $a_2$  were fitted with a flat distribution in the region of  $1.18 \leq \alpha_{2N} \leq 1.33$ . Only statistical and point-to-point uncertainties were included in the fit; scale uncertainties were applied directly to  $a_2$ .

2N-SRCs in nucleus  $A$  compared to that in  ${}^2\text{H}$ . This includes corrections related to binding differences as well as the center-of-mass motion of the 2N-SRC pairs in the  $A > 2$  nucleus [15, 29]. Table 3 shows the extracted values of  $a_2$ , obtained by fitting the plateau region for  $1.4 \leq x \leq 1.75$  ( $1.18 \leq \alpha_{2N} \leq 1.33$ ). As shown in Fig. 6,  $a_2({}^3\text{He})$ ,  $a_2({}^4\text{He})$ , and  $a_2({}^{12}\text{C})$  are consistent with previous measurements within their errors. The values of  $a_2({}^{40}\text{Ca})$  and  $a_2({}^{48}\text{Ca})$  are newly available in this work, and their similar values confirm that the nucleons in the minority (protons) primarily determine the probabilities for forming SRC pairs.

### 3.3. $A^\beta\text{He}$ Cross Section Ratios

Similarly,  $\alpha_{3N}$  has been proposed for examining scattering in the region of potential 3N-SRC contributions [32]:

$$\alpha_{3N} = 3 - \frac{q_- + 3M}{2M} \left[ 1 + \frac{m_s^2 - M^2}{W_{3N}^2} + \sqrt{\left( 1 - \frac{(m_s + M)^2}{W_{3N}^2} \right) \left( 1 - \frac{(m_s - M)^2}{W_{3N}^2} \right)} \right] \quad (5)$$

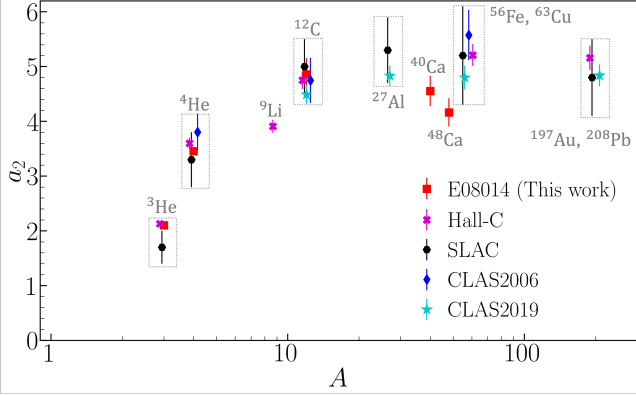


Figure 6:  $a_2$  vs.  $A$  where new results (red squares) are from Table 3, and the  $a_2$  values from the previous experiments [15, 11, 14, 17] are taken from the updated values in Ref. [10]. Different  $a_2$  values for the same  $A$  were shifted slightly for better visualization. A table of  $a_2$  values from all experiments is included in the supplemental material [39].

where  $W_{3N}^2 = \sqrt{-Q^2 + 6Mv + 9M^2}$ ,  $m_S^2 = 4 \frac{m_N^2 + k_\perp^2}{\beta(2-\beta)}$  with  $k_\perp$  being the transverse component of the relative momentum of the spectator nucleons with respect to the total spectator momentum  $\vec{p}_S$ .  $\beta$  is the light-cone momentum fraction of  $p_S$  carried by one of the spectator nucleons and is scaled to be  $0 \leq \beta \leq 2$ . In our examination of 3N-SRCs, we take  $k_\perp = 0$  and  $\beta = 1$  when calculating  $\alpha_{3N}$  to represent the linear configurations that are expected to be dominant [32, 20].

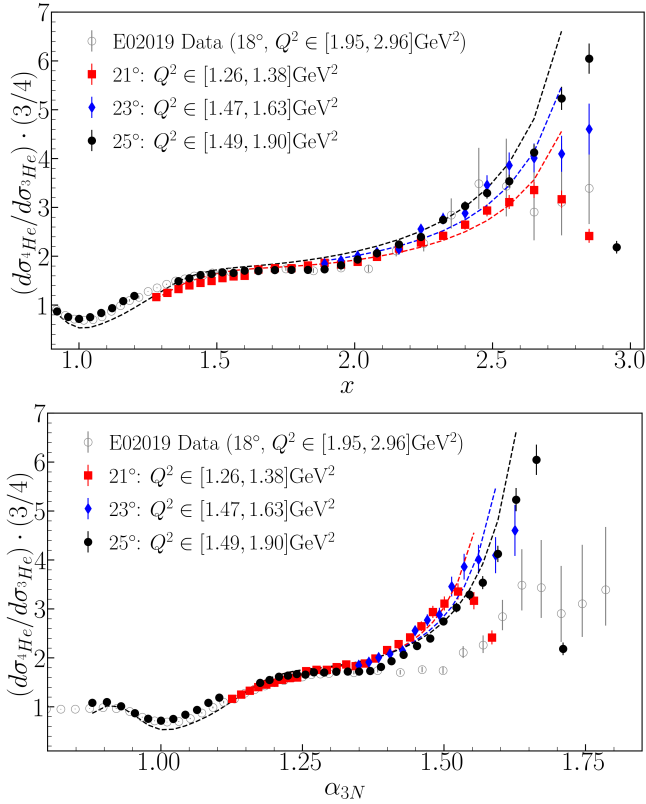


Figure 7: The  ${}^4\text{He}/{}^3\text{He}$  ratio of the cross section per nucleon as a function of  $x$  (top)  $\alpha_{3N}$  (bottom) for all angles. Data are from this work and Ref. [15]. Scale uncertainties are not shown.

Figure 7 shows the  ${}^4\text{He}/{}^3\text{He}$  ratios at all scattering angles

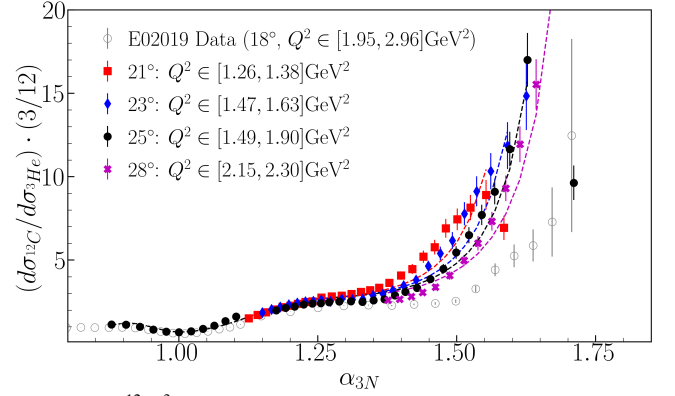


Figure 8: The  ${}^{12}\text{C}/{}^3\text{He}$  ratio of the cross section per nucleon as a function of  $x$  (top)  $\alpha_{3N}$  (bottom) for all angles. Data are from this work and Ref. [15]. Scale uncertainties are not shown.

as a function of  $x$  and  $\alpha_{3N}$ , including the E02-019 results at higher  $Q^2$  for comparison [15]. As reported in Ref. [16] which shows the  ${}^4\text{He}/{}^3\text{He}$  ratio with combined  $23^\circ$  and  $25^\circ$  data, there is no indication of the onset of a 3N-SRC plateau, but instead, a rapid increase is observed for  $x > 2$  ( $\alpha_{3N} > 1.41$ ). This was unexpected as nearly all of the scaling violating effects - FSI, CM motion, and binding of the 2N-SRC - have been seen to decrease with  $Q^2$  in detailed scaling studies for 2N-SRCs [11, 13, 20]. However, at these  $Q^2$  values the difference between  $x$  and  $\alpha_{3N}$  is strongly  $Q^2$  dependent, and with the rapid rise of the  ${}^4\text{He}/{}^3\text{He}$  ratios at large  $x$  values, even a modest shift between data sets going from  $x$  to  $\alpha_{3N}$  has a significant impact. When examined as a function of  $\alpha_{3N}$ , the data are more consistent with previous expectations, with the cross section ratios at  $\alpha_{3N} > 1.4$  as  $Q^2$  increases (except for points corresponding to  $x \approx 3$ , where nuclear elastic contributions enhance the denominator). This can be seen even more clearly in the  ${}^{12}\text{C}/{}^3\text{He}$  ratios shown in Fig. 8, where there is an additional data set at higher  $Q^2$ . This new examination of the  $Q^2$  dependence for the large- $\alpha_{3N}$  data supports the argument that larger  $Q^2$  values are needed to try and isolate 3N-SRCs [9, 30, 32, 33].

The cross section ratios of  $A$  to  ${}^2\text{H}$  ( ${}^3\text{He}$ ) as functions of  $x$  and  $\alpha_{2N}$  ( $\alpha_{3N}$ ) are shown in the supplemental materials [39] for all of the targets measured in this experiment.

#### 4. Conclusion

In this work, we presented the complete set of cross sections and ratios from inclusive quasi-elastic scattering data obtained in Jefferson Lab experiment E08-014, examining nuclei ranging from  ${}^2\text{H}$  to  ${}^{48}\text{Ca}$ . We find a plateau in the  $A^2/H$  ratios for  $x > 1.4$  ( $\alpha_{2N} > 1.18$ ), consistent with previous data and predictions based on the dominance of 2N-SRCs. No 3N-SRC plateau was observed in the  ${}^4\text{He}/{}^3\text{He}$  and  ${}^{12}\text{C}/{}^3\text{He}$  ratios at  $x > 2$ , where the coverage in  $\alpha_{2N}$  was limited to  $\alpha_{2N} \lesssim 1.6$ , slightly below the region where recent predictions suggest 3N-SRCs may dominate [32, 30]. While the  ${}^4\text{He}/{}^3\text{He}$  ratios taken vs  $x$  appear to be moving away from the predicted plateau as  $Q^2$  increases [34], the  $A^3/H$  ratios decrease with increasing  $Q^2$ , especially for  ${}^{12}\text{C}$  where the  $Q^2$  range is larger, consistent with an approach to the

predicted 3N-SRC dominance. The fact that the data are approaching the high- $Q^2$ , but limited precision Hall C data [15] suggests that high-precision measurements at larger  $Q^2$  values, such as those taken by JLab experiment E12-06-105 [42] may be able to isolate the presence of 3N-SRCs.

## Acknowledgments

We gratefully acknowledge the exceptional support from the Hall A technical staff and the JLab target group. This work was partially supported by the Department of Energy's Office of Science, Office of Nuclear Physics, under Contracts No. DE-AC05-06OR23177, DE-AC02-05CH11231, DE-AC02-06CH11357, and DE-FG02-96ER40950, as well as by the National Science Foundation. Additional support under DOE Contract No. DE-AC05-06OR23177 was provided through JSA, LLC, which operates JLab. Y.P. Zhang and Z.H. Ye acknowledge support from the National Science Foundation of China under contract 12275148 and 12361141822. A. Shahinyan acknowledge support from the Grant 21AG-1C085 by the Science Committee of the Republic of Armenia. The  $^{48}\text{Ca}$  isotope used in this research was supplied by the Isotope Program within the Office of Nuclear Physics in the Department of Energy's Office of Science. Finally, we remember and honor Patricia Solvignon, who was instrumental in the development of Experiment E08-014; her passing is deeply felt by our community.

## References

- [1] L. Lapikas, G. van der Steenhoven, L. Frankfurt, M. Strikman, M. Zhalov, The Transparency of C-12 for protons, *Phys. Rev. C* 61 (2000) 064325. [arXiv:nucl-ex/9905009](#), [doi:10.1103/PhysRevC.61.064325](#).
- [2] M. M. Sargsian, et al., Hadrons in the nuclear medium, *J. Phys. G* 29 (2003) R1. [arXiv:nucl-th/0210025](#), [doi:10.1088/0954-3889/29/3/201](#).
- [3] J. Arrington, A. Daniel, D. Day, N. Fomin, D. Gaskell, P. Solvignon, A detailed study of the nuclear dependence of the EMC effect and short-range correlations, *Phys. Rev. C* 86 (2012) 065204. [arXiv:1206.6343](#), [doi:10.1103/PhysRevC.86.065204](#).
- [4] R. Dalal, I. J. D. MacGregor, Nucleon-nucleon correlations inside atomic nuclei: synergies, observations and theoretical models, *Rept. Prog. Phys.* 87 (2024) 034301. [doi:10.1088/1361-6633/ad27dd](#).
- [5] L. L. Frankfurt, M. I. Strikman, Hard Nuclear Processes and Microscopic Nuclear Structure, *Phys. Rept.* 160 (1988) 235. [doi:10.1016/0370-1573\(88\)90179-2](#).
- [6] J. Arrington, D. W. Higinbotham, G. Rosner, M. Sargsian, Hard probes of short-range nucleon-nucleon correlations, *Prog. Part. Nucl. Phys.* 67 (2012) 898. [arXiv:1104.1196](#), [doi:10.1016/j.pnpnp.2012.04.002](#).
- [7] C. Ciofi degli Atti, In-medium short-range dynamics of nucleons: Recent theoretical and experimental advances, *Phys. Rept.* 590 (2015) 1–85. [doi:10.1016/j.physrep.2015.06.002](#).
- [8] O. Hen, G. A. Miller, E. Piasetzky, L. B. Weinstein, Nucleon-Nucleon Correlations, Short-lived Excitations, and the Quarks Within, *Rev. Mod. Phys.* 89 (2017) 045002. [arXiv:1611.09748](#), [doi:10.1103/RevModPhys.89.045002](#).
- [9] N. Fomin, D. Higinbotham, M. Sargsian, P. Solvignon, New Results on Short-Range Correlations in Nuclei, *Ann. Rev. Nucl. Part. Sci.* 67 (2017) 129. [arXiv:1708.08581](#), [doi:10.1146/annurev-nucl-102115-044939](#).
- [10] J. Arrington, N. Fomin, A. Schmidt, Progress in understanding short-range structure in nuclei: an experimental perspective, *Ann. Rev. Nucl. Part. Sci.* 72 (2022) 307. [arXiv:2203.02608](#), [doi:10.1146/annurev-nucl-102020-022253](#).
- [11] L. L. Frankfurt, M. I. Strikman, D. B. Day, M. Sargsian, Evidence for short range correlations from high  $Q^2$  (e, e-prime) reactions, *Phys. Rev. C* 48 (1993) 2451. [doi:10.1103/PhysRevC.48.2451](#).
- [12] J. Arrington, et al., Inclusive electron - nucleus scattering at large momentum transfer, *Phys. Rev. Lett.* 82 (1999) 2056. [arXiv:nucl-ex/9811008](#), [doi:10.1103/PhysRevLett.82.2056](#).
- [13] K. S. Egiyan, et al., Observation of nuclear scaling in the A(e, e') reaction at  $x_B > 1$ , *Phys. Rev. C* 68 (2003) 014313. [arXiv:nucl-ex/0301008](#), [doi:10.1103/PhysRevC.68.014313](#).
- [14] K. S. Egiyan, et al., Measurement of 2- and 3-nucleon short range correlation probabilities in nuclei, *Phys. Rev. Lett.* 96 (2006) 082501. [arXiv:nucl-ex/0508026](#), [doi:10.1103/PhysRevLett.96.082501](#).
- [15] N. Fomin, et al., New measurements of high-momentum nucleons and short-range structures in nuclei, *Phys. Rev. Lett.* 108 (2012) 092502. [arXiv:1107.3583](#), [doi:10.1103/PhysRevLett.108.092502](#).
- [16] Z. Ye, et al., Search for three-nucleon short-range correlations in light nuclei, *Phys. Rev. C* 97 (2018) 065204. [doi:10.1103/PhysRevC.97.065204](#).
- [17] B. Schmookler, et al., Modified structure of protons and neutrons in correlated pairs, *Nature* 566 (2019) 354. [arXiv:2004.12065](#), [doi:10.1038/s41586-019-0925-9](#).
- [18] D. Nguyen, et al., Novel observation of isospin structure of short-range correlations in calcium isotopes, *Phys. Rev. C* 102 (2020) 064004. [doi:10.1103/PhysRevC.102.064004](#).
- [19] S. Li, et al., Revealing the short-range structure of the mirror nuclei  $^3\text{H}$  and  $^3\text{He}$ , *Nature* 609 (2022) 41. [doi:10.1038/s41586-022-05007-2](#).
- [20] S. Li, et al., Inclusive studies of two- and three-nucleon short-range correlations in  $^3\text{H}$  and  $^3\text{He}$ , *arXiv:2404.16235* (2024).
- [21] A. Tang, J. W. Watson, J. Aclander, J. Alster, G. Asryan, et al., n-p short range correlations from (p,2p + n) measurements, *Phys. Rev. Lett.* 90 (2003) 042301. [arXiv:nucl-ex/0206003](#), [doi:10.1103/PhysRevLett.90.042301](#).
- [22] R. Shneur, et al., Investigation of proton-proton short-range correlations via the C-12(e, e' pp) reaction, *Phys. Rev. Lett.* 99 (2007) 072501. [arXiv:nucl-ex/0703023](#), [doi:10.1103/PhysRevLett.99.072501](#).
- [23] R. Subedi, et al., Probing Cold Dense Nuclear Matter, *Science* 320 (2008) 1476. [arXiv:0908.1514](#), [doi:10.1126/science.1156675](#).
- [24] I. Korover, et al., Probing the Repulsive Core of the Nucleon-Nucleon Interaction via the  $^4\text{He}(e,e'pN)$  Triple-Coincidence Reaction, *Phys. Rev. Lett.* 113 (2014) 022501. [arXiv:1401.6138](#), [doi:10.1103/PhysRevLett.113.022501](#).
- [25] M. Duer, et al., Direct Observation of Proton-Neutron Short-Range Correlation Dominance in Heavy Nuclei, *Phys. Rev. Lett.* 122 (2019) 172502. [arXiv:1810.05343](#), [doi:10.1103/PhysRevLett.122.172502](#).
- [26] R. Schiavilla, R. B. Wiringa, S. C. Pieper, J. Carlson, Tensor Forces and the Ground-State Structure of Nuclei, *Phys. Rev. Lett.* 98 (2007) 132501. [arXiv:nucl-th/0611037](#), [doi:10.1103/PhysRevLett.98.132501](#).
- [27] M. Alvioli, C. Ciofi degli Atti, H. Morita, Proton-neutron and proton-proton correlations in medium-weight nuclei and the role of the tensor force, *Phys. Rev. Lett.* 100 (2008) 162503. [doi:10.1103/PhysRevLett.100.162503](#).
- [28] A. Schmidt, et al., Probing the core of the strong nuclear interaction, *Nature* 578 (2020) 540. [arXiv:2004.11221](#), [doi:10.1038/s41586-020-2021-6](#).
- [29] R. Weiss, A. W. Denniston, J. R. Pybus, O. Hen, E. Piasetzky, et al., Extracting the number of short-range correlated nucleon pairs from inclusive electron scattering data, *Phys. Rev. C* 103 (2021) L031301. [arXiv:2005.01621](#), [doi:10.1103/PhysRevC.103.L031301](#).
- [30] D. B. Day, L. L. Frankfurt, M. M. Sargsian, M. I. Strikman, Toward observation of three-nucleon short-range correlations in high- $Q^2$  A(e,e')X reactions, *Phys. Rev. C* 107 (2023) 014319. [arXiv:1803.07629](#), [doi:10.1103/PhysRevC.107.014319](#).
- [31] D. Higinbotham, E. Piasetzky, M. Strikman, Protons and neutrons cosy up in nuclei and neutron stars, *CERN Cour.* 49N1 (2009) 22–24.
- [32] M. M. Sargsian, D. B. Day, L. L. Frankfurt, M. I. Strikman, Searching for three-nucleon short-range correlations, *Phys. Rev. C* 100 (2019) 044320. [arXiv:1910.14663](#), [doi:10.1103/PhysRevC.100.044320](#).
- [33] N. Fomin, J. Arrington, S. Li, Searching for three-nucleon short-range correlations, *Eur. Phys. J. A* 59 (2023) 205. [arXiv:2309.03963](#), [doi:10.1146/annurev-nucl-102020-022253](#).

- [10.1140/epja/s10050-023-01112-6](https://doi.org/10.1140/epja/s10050-023-01112-6).
- [34] Z. Ye, J. Arrington, Inclusive Studies of Short-Range Correlations: Overview and New Results, Proceedings of the 13th Conference on the Intersections of Particle and Nuclear Physics, arXiv:1810.03667 (2018).
- [35] H. Baghdasaryan, et al., Tensor Correlations Measured in  ${}^3\text{He}(e, e'pp)n$ , Phys. Rev. Lett. 105 (2010) 222501. [arXiv:1008.3100](https://arxiv.org/abs/1008.3100), [doi:10.1103/PhysRevLett.105.222501](https://doi.org/10.1103/PhysRevLett.105.222501).
- [36] Z. Ye, Short Range Correlations in Nuclei at Large  $x_{bj}$  through Inclusive Quasi-Elastic Electron Scattering, Ph.D. thesis, Physics - Graduate School of Arts and Sciences, University of Virginia (2013). [arXiv:1408.5861](https://arxiv.org/abs/1408.5861), [doi:10.18130/V3FJ7H](https://doi.org/10.18130/V3FJ7H).
- [37] P. Solvignon-Slifer, J. Arrington, D. Day, D. Higinbotham, [E08-014: Three-nucleon short range correlation studies in inclusive scattering for  \$0.8 < Q^2 < 2.8 \text{ GeV}^2\$](#) . (2008).  
URL [http://www.jlab.org/exp\\_prog/proposals/08/PR-08-014.pdf](http://www.jlab.org/exp_prog/proposals/08/PR-08-014.pdf)
- [38] J. Alcorn, et al., Basic Instrumentation for Hall A at Jefferson Lab, Nucl. Instrum. Meth. A 522 (2004) 294. [doi:10.1016/j.nima.2003.11.415](https://doi.org/10.1016/j.nima.2003.11.415).
- [39] See Supplemental Material at [URL will be inserted by publisher] for detailed expressions and tables of cross section results. (2025).
- [40] S. Dasu, et al., Measurement of kinematic and nuclear dependence of  $R = \sigma_L / \sigma_T$  in deep inelastic electron scattering, Phys. Rev. D 49 (1994) 5641. [doi:10.1103/PhysRevD.49.5641](https://doi.org/10.1103/PhysRevD.49.5641).
- [41] S. Moran, M. Arratia, J. Arrington, D. Gaskell, B. Schmookler, Significance of radiative corrections on measurements of the EMC effect, Phys. Rev. C 110 (2024) 025202. [doi:10.1103/PhysRevC.110.025202](https://doi.org/10.1103/PhysRevC.110.025202).
- [42] J. Arrington, D. Day, N. Fomin, P. Solvignon-Slifer, [E12-06-105: Inclusive Scattering from Nuclei at  \$x > 1\$  in the quasielastic and deeply inelastic regimes](#) (2006).  
URL [www.jlab.org/exp\\_prog/proposals/06/PR12-06-105.pdf](http://www.jlab.org/exp_prog/proposals/06/PR12-06-105.pdf)